Environmental Science Nano

Accepted Manuscript

This article can be cited before page numbers have been issued, to do this please use: S. Panneri, P. Ganguly, B. N. Nair, A. M. Peer, K.G.K. Warrier and H. U. N. Saraswathy, *Environ. Sci.: Nano*, 2016, DOI: 10.1039/C6EN00410E.

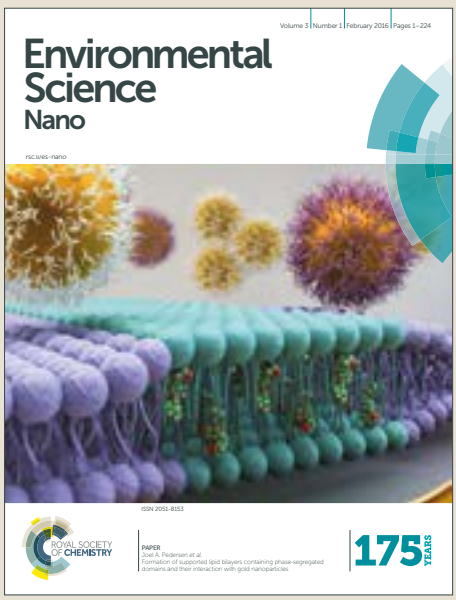

ROYAL SOCIETY OF CHEMISTRY

rsc.li/es-nano

View Article Online
DOI: 10.1039/C6EN00410E

Environmental Significance Statement

The widespread industrial use of organic compounds like pharmaceuticals, antibiotics, and textile dyes has in recent times, posed a major threat to the environment due to issues associated with its degradation and safe disposal. Consequently, we are faced with the emergence of newer hazards, like drug resistant bacteria, that warrant immediate remedial measures. The greener approach for the alleviation of such issues is the use of sunlight active photocatalysts with appreciable efficiencies and recyclability. The technique is superior to adsorption as photocatalysis does not necessitate secondary remediation measures for the disposal of pollutants. In the present work, Co_3O_4-C_3N_4 p-n nano-heterojunctions, obtained by a simple one pot synthetic strategy for the first time, are demonstrated to be efficient photocatalysts for the simultaneous degradation of a mixture of environmental pollutants like tetracycline antibiotic and methylene blue dye. The ultrafine dispersions of nanosized Co_3O_4 particles in C_3N_4 sheets lead to the formation of intimate interfaces that induced synergy in visible light absorption and reduced exciton combinations for enhanced photo physical properties. This template free approach, eliminating the use of fluorinated acids, also provided ten- fold increase in surface area values providing good photocatalytic efficiencies.

View Article Online
DOI: 10.1039/C6EN00410E

Journal Name

ARTICLE

Co_3O_4-C_3N_4 p-n nano-heterojunctions for the simultaneous degradation of a mixture of pollutants under solar irradiation

Received 00th January 20xx,
Accepted 00th January 20xx

DOI: 10.1039/x0xx00000x

www.rsc.org/

P. Suyana,[ab] Priyanka Ganguly, [a] Balagopal N. Nair,[cd] A. Peer Mohamed, [a] K. G. K. Warrier [a] and U. S. Hareesh [ab]*

Environmental remediation employing sun light active semiconductor nano heterostructures provide effective solutions for handling emerging contaminants through a greener approach. Herein, we report, the creation of ultrafine dispersions of Co_3O_4 nanoparticles in g-C_3N_4 matrix by a simple one-pot synthetic strategy involving the co-pyrolysis of constituent raw materials. A homogeneous mixture of melamine and cobalt nitrate fired at 550°C/2h lead to the formation of Co_3O_4-C_3N_4 p-n nano heterojunctions that displayed extended absorption in the visible wavelength region owing to the synergistic role of Co_3O_4 particles. Moreover, the surface area values of the composites reached 90 m^2/g, a tenfold increase from the value of 8 m^2/g obtained for the pristine C_3N_4. The band bending, induced by the nano p-n heterojunctions, lead to the formation of intimate interfaces having enhanced photophysical properties. The mass normalized photoluminescence spectra of heterojunctions indicated reduced exciton recombinations that are validated further by the enhanced sun light induced photocatalytic degradation of a mixture of methylene blue and tetracycline organic pollutants.

Introduction

The uncontrolled disposal of organic effluents like pharmaceuticals, dyes, pesticides, organic compounds etc. into aquatic sources is a clear cause of environmental pollution that warrants immediate remedial measures.[1, 2] Of the various strategies emerging, photocatalytic degradation of organic pollutants by semiconductor nanoparticles offers a green and environment friendly solution.[3, 4] Consequently, a significant amount of work has been carried out utilizing metal oxide nanoparticles like Titania, ZnO, NiO, BiOX, Halloysite nanotubes for the photocatalytic applications in the past decade.[5-10] However, owing to band gap constraints and lower efficiencies, the widespread use of such photocatalysts could not be realized for a larger application like environmental remediation. More recently, the emergence of visible light active photocatalysts has infused renewed interest in the quest for clean and economical solutions for pollution control. Graphitic carbon nitride (g-C_3N_4) a n-type semiconductor, with a medium band gap of about 2.7 eV, is relatively a new entrant in the domain of visible active photocatalysts.[11, 12] The ease of synthesis from inexpensive precursors, high chemical and thermal stability, and the band gap compatibility with other semiconductors are the primary attributes that attracted researchers to pursue applications of C_3N_4 for diverse applications ranging from photocatalytic water splitting to sensors.[13, 14] Despite such appealing potential, C_3N_4 suffers from the major shortcomings of low visible light utilization, fast recombination of photogenerated excitons and low specific surface area.[15] Varied methods are therefore attempted to address these deficiencies and strategies like surface modification, morphological advancements, doping of metal species, composite formation, sensitizing with organic dyes etc are explored currently.[16-19] Amongst these methods, composite formation leading to heterostructures through intimate interfaces of g-C_3N_4 with metal oxides, sulphides, halides and noble metals have shown promises through improvements in photophysical properties.[12, 20] Subsequently, g-C_3N_4 has been coupled with several metal oxides such as TiO_2, ZnO, WO_3, Cu_2O, In_2O_3, Fe_2O_3, $BiVO_4$ etc. to form g-C_3N_4/ metal heterojunctions.[21-27]

Cobalt oxide (Co_3O_4) is a visibly active p-type semiconductor with attractive electronic and structural properties. Several p-n heterojunctions of Co_3O_4 with other semiconductors like TiO_2, $BiVO_4$, etc are reported to have enhanced photocatalytic activity due to reduced electron hole recombinations at the p-n junction interfaces.[28-30] The creation of p-n heterojunction leads to band bending and generation of internal electric field due to which the exciton recombinations are reduced.[31-34] Due to its favorable band alignment, Co_3O_4 is a potential metal oxide to form p-n heterostructure with g-C_3N_4. Co_3O_4 loaded on the mesoporous g-C_3N_4 surface was evaluated for the

[a]Materials Science and Technology Division, National Institute for Interdisciplinary Science and Technology (CSIR-NIIST), Thiruvananthapuram - 695019, India.
[b]Academy of Scientific and Innovative Research (AcSIR), New Delhi, India
[c]R&D Center, Noritake Co. Limited, Aichi 470-0293, Japan
[d]Nanochemistry Research Institute , Department of Chemistry, Curtin University, GPO Box UI987, Perth, WA 6845, Australia
E-mail: hareesh@niist.res.in, ushareeshnair@gmail.com
Fax: 0471 2491712, Tel: 9446337222, 0471 2535504
Electronic Supplementary Information (ESI) available: [details of any supplementary information available should be included here]. See DOI: 10.1039/x0xx00000x

View Article Online
DOI: 10.1039/C6EN00410E

photocatalytic evolution of oxygen from water as well as for the photocatalytic degradation of organic compounds.[35, 36] However, the synthesis of mesoporous layers of g-C_3N_4 sheets involved a silica templating method and employing fluorinated solvents for the post- synthesis etching process made it time consuming and environmentally hazardous. Guo et al. synthesized Co_3O_4–C_3N_4 by a two-step calcination technique using a mechanical mixture of Co_3O_4 and g-C_3N_4 wherein Co_3O_4 content was too low (below 2 wt %).[37] The reported works are thus far of processing strategies that are cumbersome and less efficient. It is therefore imperative to develop simple synthetic approaches that lead to dispersions of nano Co_3O_4 on C_3N_4 sheets. In a recent and notable contribution, Dontsova et al. synthesized C_3N_4-Co_3O_4-Co(III) Complex by the one step thermal condensation of dicyandiamide with Co(II) chloride-containing salt melts at 550 °C in flowing N_2 atmosphere. The non-porous solids thus obtained are demonstrated to be useful for water oxidation and Rhodamine b degradation.[38] Here in this study, we further supplement the one step synthesis strategy to arrive at phase pure Co_3O_4-C_3N_4 systems, for the first time, by a suitable choice of precursors and pyrolysis conditions. Co_3O_4-C_3N_4 (CC) p-n heterojunctions containing ultrafine dispersions of Co_3O_4 in C_3N_4 sheets are prepared by co-pyrolysing a homogeneous mixture of the precursors, melamine, and cobalt nitrate in air at 550 °C. The composite formed showed improved sun light driven photocatalytic activity and the efficiency was evaluated by analyzing the degradation of a mixture of organic compounds (Antibiotic + Dye) as a case study on water pollution.

Experimental

Synthesis

Pristine g-C_3N_4 is prepared by the thermal condensation and evaporation of melamine and pure Co_3O_4 is obtained by the thermal decomposition of cobalt nitrate at 550 °C at a ramping rate of 3 °C for 2 hrs in air atmosphere. In a typical synthesis, Co_3O_4-C_3N_4 composites are prepared using a one-pot synthetic approach by mixing 4g melamine with different ratio of cobalt nitrate (0.1g, 0.4g, and 0.7g) and heated at 550 °C in air at a ramping rate of 3 °C for 2 hrs. The as-synthesised composites are correspondingly designated as CC0.1, CC0.4, and CC0.7 and used as such for characterization and photocatalytic application. For a comparative evaluation, mechanical mixture Co_3O_4-C_3N_4 (4:96 by weight) composite is prepared by homogeneously mixing the constituent powders in agate mortar and denoted hereafter as CCM.

Photocatalytic degradation studies

The photocatalytic activity of the prepared samples is evaluated by the sunlight induced degradation of a mixture of the organic effluents; methylene blue (MB) and tetracycline (TC). About 500 mg/L photocatalyst is added to a mixture containing 10^{-5} M MB and 10^{-4} M TC and stirred in dark for 30 minutes, prior to irradiation, to attain the adsorption-desorption equilibrium. The reaction mixture is then irradiated under sunlight and the suspension is collected at regular intervals of 30 minutes for measuring the changes in the concentration of MB (664 nm) and TC (357 nm) using a UV-Vis spectrophotometer. The individual degradation of MB and TC is also studied for comparison.

Result and Discussion

The composition and thermal stability of g-C_3N_4 and the different compositions of Co_3O_4- C_3N_4 composites are evaluated by a post-synthesis thermogravimetric analysis (TGA) in the temperature range of 50° to 850° C in air atmosphere at a rate of 3 °C/ min. Figure 1, providing the decomposition profiles of the samples, indicates that the pure g-C_3N_4 decomposes completely at T >600°C while nearly 4 wt% residue (Co_3O_4) is left for the composite CC0.1 sample. The other two composites (CC0.4 and CC0.7) left behind 15 wt% and 97 wt% of Co_3O_4 residue respectively. The weight retained indicates the amount of Co_3O_4 content in the composite samples and the prepared composites are therefore estimated to be of C_3N_4-4 wt% Co_3O_4 (CC0.1), C_3N_4-15 wt% Co_3O_4 (CC0.4), C_3N_4-97 wt% Co_3O_4 (CC0.7) compositions. The most notable aspect of the thermal analysis is the early thermal degradation (at T<400°C) observed in CC0.1 and CC0.4 composite samples. Incorporation of Co_3O_4 nanoparticles on C_3N_4 sheets improves the surface area by ten folds (presented in detail on the results of BET) and is believed to induce oxidative etching of C_3N_4 sheets leading to an early weight loss compared to the bulk C_3N_4.

The powder XRD patterns of the as prepared g-C_3N_4, Co_3O_4, mechanical mixture CCM and Co_3O_4-C_3N_4 composite (CC0.1, CC0.4 and CC0.7) samples are shown in Figure 2. The pristine g-C_3N_4 is characterised by well defined peaks at 27.4° and 13.1° owing to the (100) and (002) diffraction planes corresponding to the interplanar stacking of aromatic systems and the interlayer structural packing respectively.[11] The peaks of pure Co_3O_4 are of the cubic spinel type structure at 2θ values of 18.90°, 31.29°, 36.81°, 38.54°, 44.80°, 59.37°, 65.27°

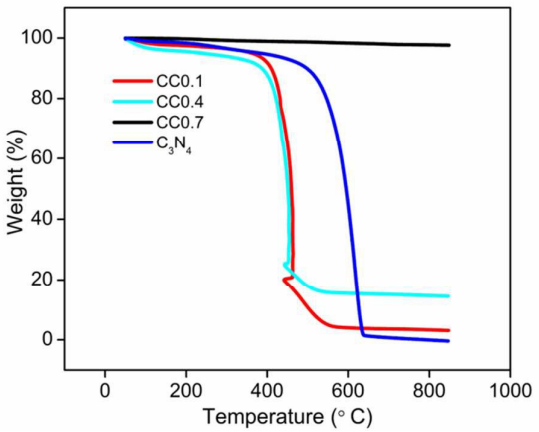

Fig. 1 Thermal decomposition patterns of g-C_3N_4 and Co_3O_4-C_3N_4 compositions.

View Article Online
DOI: 10.1039/C6EN00410E

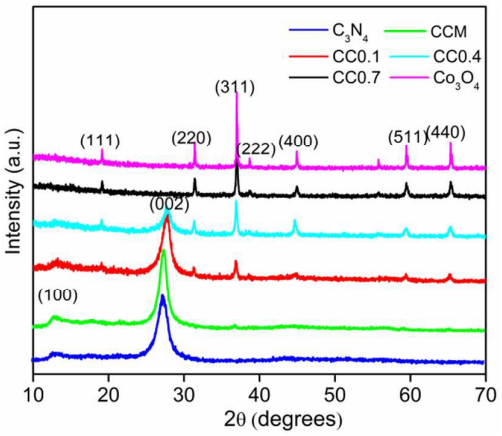

Fig. 2 XRD patterns of the as prepared Co_3O_4- C_3N_4 (CC) composites, g-C_3N_4, Co_3O_4, and mechanical mixture CCM.

corresponding to (111), (220), (311), (222), (400), (511) and (440) planes respectively (JCPDS-00-042-1467).[28] The XRD pattern of CC0.1 (C_3N_4-4 wt% Co_3O_4) shows peaks of both g-C_3N_4 and Co_3O_4. The increase in Co_3O_4 content reduces the peak intensities of g-C_3N_4 in CC0.4 (C_3N_4-15 wt% Co_3O_4). The CC0.7 (C_3N_4-97 wt% Co_3O_4) composite is dominantly Co_3O_4 phase with no peaks for the g-C_3N_4 phase as has been substantiated by the TGA analysis. It is presumed that the increase in cobalt nitrate in the precursor mix can lead to significant release of nitrate fumes due to which there is considerable loss of C_3N_4 from the composition of CC0.7. The mechanical mixture CCM shows predominantly peaks of C_3N_4 and a minor peak at 36.81° represent (311) plane of Co_3O_4 indicating inhomogeneous distribution of Co_3O_4 phase and presumably lack heterostructure formation.

The TEM images of pristine C_3N_4 and Co_3O_4 are shown in Figure 3 (a-b). Thick planar aggregates of g-C_3N_4 sheets are observed in Figure 3 (a) while Figure 3 (b) revealed irregularly shaped Co_3O_4 particles of above 50 nm when synthesized separately without C_3N_4. In Figure 3 c and d, exfoliated planar sheets of g-C_3N_4 are seen decorated with dark dots, corresponding to

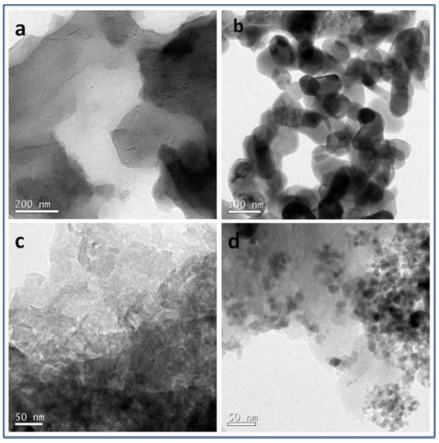

Fig. 3 TEM images of (a) g-C_3N_4, (b) Co_3O_4, (c) and (d) Co_3O_4-C_3N_4 (CC0.1) composite.

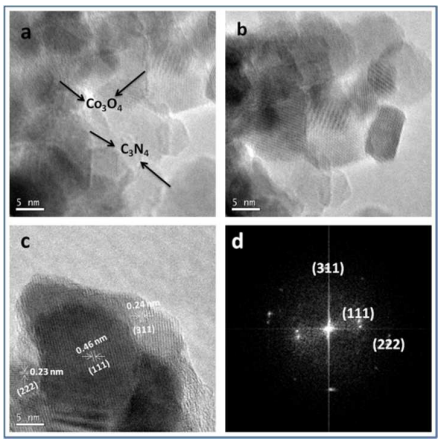

Fig. 4 HRTEM images of Co_3O_4-C_3N_4 (CC) composite.

Co_3O_4 nanoparticles of 10-15 nm, throughout the sheets and are distinct from the pristine C_3N_4 and Co_3O_4. The size of the Co_3O_4 nanoparticles reduced significantly (10-15nm) when incorporated within C_3N_4 sheets through the one pot co-pyrolysis method adopted. The evolution of volatile products like NO_2 and NH_3 during the pyrolysis and condensation process of composite preparation can presumably restrict the growth of nanoparticles and can exfoliate the aggregated sheets of g-C_3N_4. Moreover, incorporation of ultrafine dispersions of Co_3O_4 nanoparticles in the matrix also leads to enhanced surface area. The TEM images of CC0.7 shown in Figure S1 show the presence of aggregated, micron sized Co_3O_4 particles on C_3N_4 sheets.

The EDAX of g-C_3N_4, Co_3O_4 and CC0.1 composite are shown in Figure 5 (a-c) which confirms the elemental composition of the synthesized samples. Energy-dispersive X-ray spectrum (EDS) mapping analyses from SEM of the CC composite presented in Figure 5 (d-h) illustrate the homogeneous distribution of the four elements(C, N, O, and Co) throughout the sample. This analysis substantiates that the composite is composed of only C, N, Co and O elements without any impurities. The lower content of Co_3O_4 in the composite and its near homogeneous distribution is vivid from the elemental mapping analysis.

The N_2 adsorption-desorption isotherms of CC composites and g-C_3N_4 are shown in Figure 6. The adsorption isotherms are of typical type II b (BDDT Classification) behavior and indicate adsorption in sheet like structures. The change in volume of adsorbed nitrogen (in other words porosity) between the samples is a clear indication of the influence of second phase (Co_3O_4) addition on the porous structure of C_3N_4. The porosity of C_3N_4 rich sample CC0.1 has clearly enhanced by the addition of 4 wt% of Co_3O_4. With further increase in the amount of the second phase, the adsorbed volume drops obviously indicating that the enhancement in adsorption volume was not driven solely by the very small second phase particles. The surface area values of the different CC compositions and the pure g-C_3N_4 and Co_3O_4 were calculated for a better understanding of the composite nanostructure (Table 1). The CC0.1 composite

View Article Online
DOI: 10.1039/C6EN00410E
ARTICLE Journal Name

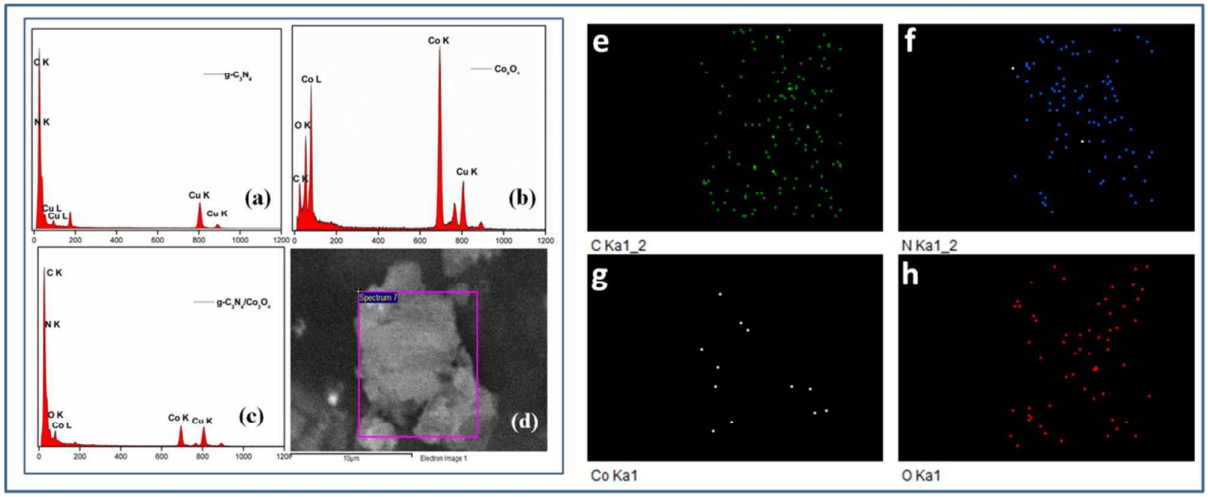

Fig. 5 EDAX of (a) g-C_3N_4 (b) Co_3O_4 and (c) Co_3O_4-C_3N_4 (CC) composite (d) SEM image showing the selected area of elemental mapping and EDS mapping of elements (e) C K, (f) N K, (g) Co K and (h) O K.

had a surface area of 90 m^2g^{-1} while pure g-C_3N_4 showed only 8 m^2g^{-1} surface area value. The surface area of the CC0.1 composite, therefore, enhanced 10 folds due to the dispersion of ultrafine Co_3O_4 nanoparticles in C_3N_4 sheets preventing aggregation. The increase in specific surface area is expected to benefit the photocatalytic degradation process. The release of volatile decomposition products (NO_2 and NH_3) during the pyrolysis process can also induce the formation of mesopores and exfoliation of sheets contributing to the enhanced surface area in composite samples.[41] However, as the Co_3O_4 content increased, the surface area values declined and reached 57 m^2/g for the CC0.4 sample and 4 m^2/g for the CC0.7 composite sample. As has been seen from TGA studies, the CC0.7 composition is 97 % by weight of Co_3O_4 and the formation of larger sized Co_3O_4 particles, in the absence of C_3N_4 sheets, should have lead to the drastic reduction in surface area values. The individually synthesized Co_3O_4 particles exhibited negligible surface area. The mechanical mixture (CCM) showed surface area of only 7 m^2/g, confirming its aggregated structure devoid of any ultrafine dispersions of nano Co_3O_4.

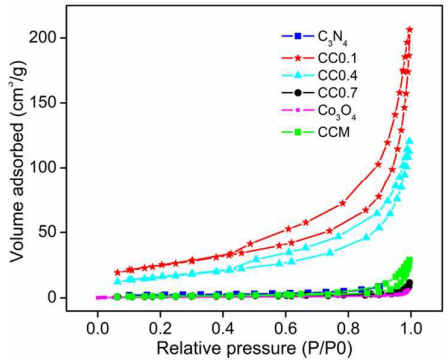

Fig. 6 N_2 adsorption-desorption isotherms of Co_3O_4-C_3N_4 (CC) composites, g-C_3N_4 Co_3O_4, and mechanical mixture CCM.

Table 1. Surface area values of C_3N_4, Co_3O_4, and Co_3O_4-C_3N_4 Composites (CC)

Sample	Surface Area (m^2/g)
C_3N_4	8
Co_3O_4	2
CC0.1	90
CC0.4	57

Hence, based on the TGA, XRD, TEM and BET surface area analysis, CC0.1 composite with a composition of C_3N_4-4 wt% Co_3O_4 is chosen as the ideal candidate for application studies and is hereafter denoted as CC unless otherwise stated.

The surface elemental analysis of each sample is obtained by XPS measurements. The survey spectrum of the composite shown in Figure 7 (a) indicates the presence of carbon, nitrogen, cobalt and oxygen. The C1s [Figure 7 (b)] spectrum shows two dominant peaks around 286.86 eV and 290.45 eV

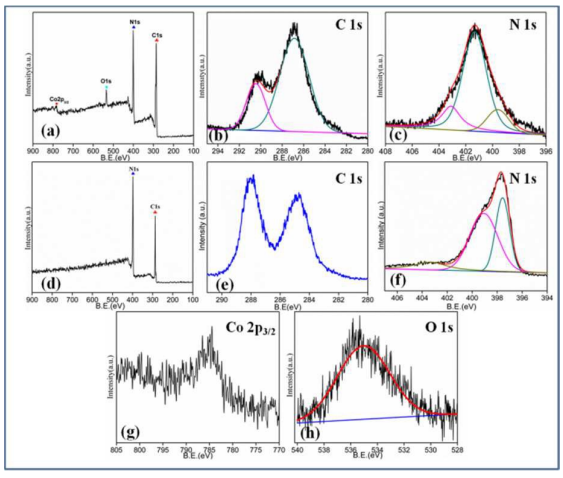

Fig. 7 (a) Survey spectrum and high-resolution XPS patterns of (b) C 1s, (c) N1s, of g-Co_3O_4- C_3N_4 (CC) composite, (d) Survey spectrum and high-resolution XPS patterns of (e) C 1s, (f) N1s, of g-C_3N_4 and (g) Co 2p and (f) O 1s of Co_3O_4.

View Article Online
DOI: 10.1039/C6EN00410E

corresponding to C=N sp^2 bonds and the interaction of Co_3O_4 with g-C_3N_4 in CC composite respectively.[37, 42] The N1s spectrum [Figure 7 (c)] of g-C_3N_4 shows three impressive peaks around 399.6, 401.3 and 403.1 eV ascribed to the C-N sp^3 bonds, C=N sp^2 bonds and to the interaction of g-C_3N_4 sheets with Co_3O_4 particles.[42] For comparison, C1s and N1s survey spectra of pristine g-C_3N_4 are shown in Figure 7 (d), 7 (e) and 7 (f). The C1s spectrum [Figure 7 (e)] of pristine g-C_3N_4 showed two dominant peaks around 284.4 and 288.1 eV. The peak at 284.4 eV is ascribed to the adventitious carbon and the peaks at 288.1 eV to N-C=N bonds, which is the major carbon species. The high resolution spectrum of N1s [Figure 7 (f)] showed two dominant peaks at 398.3 and 400.8 eV. The peak at 398.3 eV is ascribed to the C-N=C bond in triazine rings and the peak at 400.8 eV is ascribed to tertiary nitrogen N-$(C)_3$ bonds. The high resolution Co 2p spectrum shown in Figure 7 (g) indicates that the Co_3O_4 contains the mixed oxidation states of Co^{+2} and Co^{+3} at 784.3 eV and 797.1 eV respectively.[43, 44] The O1s spectrum in Figure 7 (h) show a distinct peak at 534.9 eV, which is ascribed to surface adsorbed hydroxyl or oxygen atoms.[45]

The optical absorption of the as prepared samples is measured using UV-vis absorption spectra and is presented in Figure. 8. The pristine g-C_3N_4 show absorption from UV to visible light with the main absorption edge at 440 nm and a weaker absorption tail in the visible light region.[46] The characteristic absorption edge of the C_3N_4 in CC composite showed a slight blue shift due to quantum confinement effect of the exfoliated nanosheets of C_3N_4.[47] Moreover incorporation of Co_3O_4 improved the optical absorption with a peak at around 732 nm in the visible region. This is attributed to the small band gap of Co_3O_4, which has direct transitions at 1.45 and 2.07 eV, corresponding to O^{2-} to Co^{3+} excitation and O^{2-} to Co^{2+} charge transfer respectively.[48] The enhanced visible light absorption is observed also from the change in colour of pure g-C_3N_4 from yellow to a light grayish one for the composite. The improved visible light absorption signifies the efficient coupling of the constituents and formation of effective heterostructure

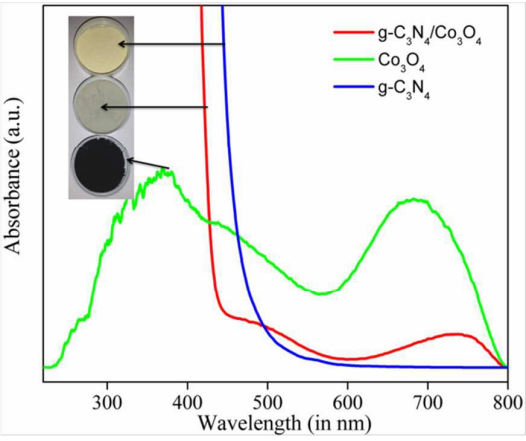

Fig. 8 UV-vis absorption spectra of Co_3O_4-C_3N_4 (CC), Co_3O_4 and g-C_3N_4.

nanocomposites. On the contrary, the mechanical mixture CCM indicated a pattern resembling that of C_3N_4 without any absorption beyond 450 nm Figure S2. The processing advantages of the one-pot synthesis are thus categorically established where the formation of intimate interfaces of Co_3O_4-C_3N_4 led to the creation of p-n nano heterojunctions with improved photophysical properties.

The FTIR spectra of CC and pristine g-C_3N_4 are shown in Figure S3. The composite preparative conditions did not affect the signature peaks of g-C_3N_4. The functional groups of g-C_3N_4 are concentrated in the 1100-1650 cm^{-1} corresponding to the stretching vibration of C-N and C=N. The absorption at 810 cm^{-1} is attributed to the breathing modes of triazine rings.[49]

Photocatalytic degradation of pollutant mixture (antibiotic + dye)

The tetracycline degradation studies of all the prepared composites in comparison with pristine C_3N_4 and Co_3O_4 is shown in Figure S4. The CC0.1 (i.e. CC) composite exhibited maximum degradation efficiency within 180 minutes of irradiation. Further, the practical application of the efficient composite (CC) is evaluated by the degradation of a mixture of organic pollutants (Antibiotic + Dye) under sunlight irradiation. The degradation profiles of the two pollutants in the mixture (MB+TC) using CC composite are elucidated from UV-vis measurements as presented in Figure S5. The intensity reduction at 360 nm corresponds to TC while that at 668 nm represents MB degradation. The photocatalyst CC effectively degraded both the pollutants from the mixture. Figure 9 (a) shows the TC degradation profile of the composite in comparison with pristine g-C_3N_4 and Co_3O_4. The prepared composite degrades more than 97% of TC within 180 mins of sunlight irradiation compared to 55% by bare g-C_3N_4 and 35% by Co_3O_4. Co_3O_4 being a p- type visible active semiconductor shows little effectiveness primarily due to its negligible specific surface area. Figure 9 (b) shows the MB degradation profile of the samples and it is seen that more than 90 % of MB is degraded by CC within 30 mins of sunlight irradiation and 100 % of MB was degraded within 90 mins of exposure. Bare g-C_3N_4 also shows 70 % of MB degradation within 180 mins of sunlight irradiation. Co_3O_4 sample indicates only 15 % of MB degradation. The degradation efficiency of the composite (CC) is significantly higher due primarily to increased surface area as observed in BET SA measurements. The reduced exciton recombination in Co_3O_4- C_3N_4 p-n heterojunctions is also a vital factor aiding increased photocatalytic efficiencies (substantiated by PL measurements discussed below). Figure 9(c) and (d) shows the C/C_0 vs time profiles of the mixture of organic pollutants (Antibiotic + Dye). TC and MB show maxima at 360 nm and 668 nm respectively and can thus be used to evaluate the concentration of these pollutants within the sample mixture. Figure 9 (c) shows the change in C/C_0 of TC in the organic mixture when irradiated for 180 mins. The composite degraded 78 % of TC from its mixture with MB in the provided span of irradiation. The degradation activity of TC

View Article Online
DOI: 10.1039/C6EN00410E

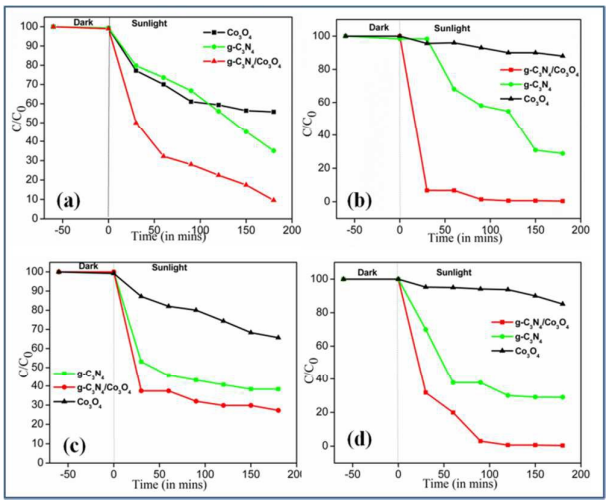

Fig. 9 (a) TC photocatalytic degradation profile (b) MB photocatalytic degradation profile (c) TC photocatalytic degradation profile in the mixture of MB+TC (d) MB photocatalytic degradation profile in the mixture of MB+TC.

is slightly reduced in the mixture when compared to its individual activity, as shown in Figure 9 (a). Similarly, Figure 9 (d) shows the change in C/C_0 of MB in the organic mixture when irradiated for 180 mins. The composite degraded 100 % of MB within 120 mins of irradiation of the mixture. The summary of % degradation efficiency of CC, C_3N_4, and Co_3O_4 are shown in Table S1. Enhanced performances are obtained for the CC heterostructures in all the cases.

The photocatalytic degradation of the organic pollutant generally is regarded as pseudo-first order kinetics and follows equation 2.1 where C_0 is in millimolar concentration.

$$\ln (C_0/C) = Kt \qquad \text{Equation (1)}$$

Where C_0 is the concentration of TC and MB after initial adsorption- desorption equilibrium, C is the concentration

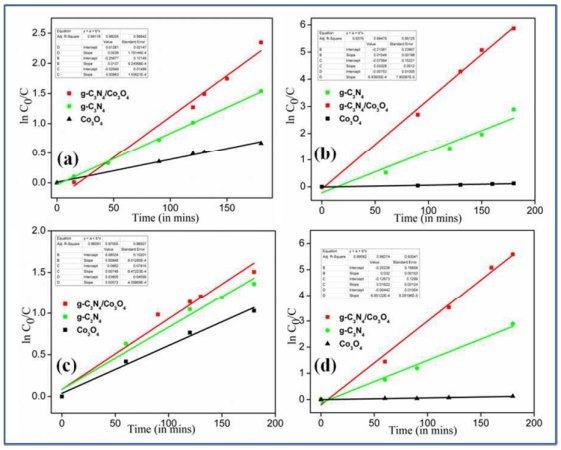

Fig. 10 (a) Rate of photocatalytic degradation of TC (b) Rate of photocatalytic degradation of MB (c) Rate of photocatalytic degradation of TC in the organic mixture (d) Rate of photocatalytic degradation of MB in the organic mixture.

Table 2. Rate constants of photocatalysts for different photocatalytic degradation.

Sample	Rate constant (min^{-1})			
	TC alone	TC in mixture	MB alone	MB in mixture
C_3N_4	0.0086	0.0074	0.0155	0.0161
Co_3O_4	0.0038	0.0057	0.0006	0.0006
CC	0.0137	0.0084	0.0333	0.0333

after visible light irradiation and K is the first order kinetics rate constant. Figure 10(a) shows the rate of photocatalytic degradation of TC using the composite in comparison with pristine g-C_3N_4 and Co_3O_4. Figure 10(b) shows the rate of photocatalytic degradation of MB using the composite. Similarly, Figure 10 (c) and (d) shows the $\ln C_0/C$ vs time plot of the mixture of organic pollutants (Antibiotic + Dye) using CC, compared along with pristine g-C_3N_4 and Co_3O_4. The slope gives the rate constant of the degradation process and Table 2 summarizes the rate constants for the different samples. The maximum rate constant in all the processes is obtained for the composite prepared (CC) which affirms its improved photocatalytic behavior. To understand the mineralization efficiency of the prepared CC heterostructure, chemical oxygen demand (COD) analysis is done using MB and it is observed that CC displayed better mineralization efficiency compared to pristine C_3N_4 (Figure S6). We have selected MB for the COD analysis as degradation products of TC yield small carbonaceous products as reported earlier.[50]

The recyclability studies of CC are performed to ascertain its stability and determine its practical viability. Figure 11 shows 5 cycles of photocatalytic degradation tests performed on a mixture of TC + MB solution. The composite shows very little change in the activity even after five cycles, suggesting excellent recyclability of the photocatalyst. Both the pollutants are effectively degraded suggesting the practical use of such heterojunctions for the treatment of discharges from pharmaceutical wastes etc. The XRD and FTIR patterns of Co_3O_4-C_3N_4 (CC) after the cyclic studies, presented in Figure S7 (a) and (b) indicated no changes in phase and functional groups respectively.

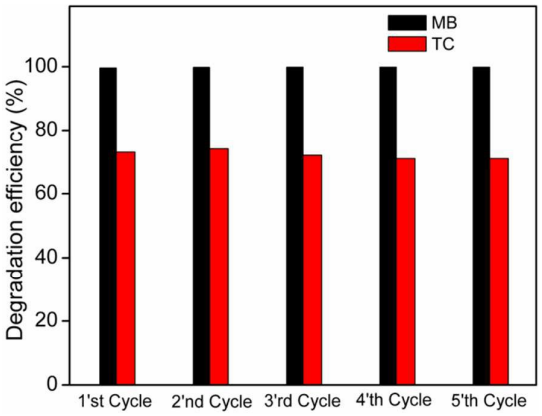

Fig. 11 (a) Recyclability of the photocatalytic degradation of MB in the organic mixture and (b) Recyclability of the photocatalytic degradation of TC in the organic mixture.

View Article Online
DOI: 10.1039/C6EN00410E

Active species formed during the photocatalytic reaction of Co_3O_4-C_3N_4 (CC) composite are presented in Figure 12. Different scavengers are employed to detect the ROS species. 10mM of Isopropanol (IPA) (as a quencher of $OH^{\cdot}$), 6mM $AgNO_3$ (as a quencher of an electron), 6mM Benzoquinone (BQ) (as a quencher of O_2^{-}) and 10mM Triethanolamine (TEA) (as a quencher of holes) are respectively added in the photocatalytic system and irradiated under sunlight.[33, 51] The photocatalytic degradation of TC is not affected by the addition of Isopropanol (IP) while the degradation is quenched drastically by the presence of Benzoquinone (BQ), triethanolamine (TEA) and partially due to $AgNO_3$. Therefore, it can be concluded that the superoxide anions (O_2^{-}), electrons and holes, are the main reactive species generated by the photocatalysts for TC degradation under sunlight irradiation.

The mass normalized photoluminescence spectrum of g-C_3N_4 and Co_3O_4-C_3N_4 composite presented in Figure 13 is used to elucidate the effect of heterojunction formation on the exciton recombination rates. The main emission peak of g-C_3N_4 and Co_3O_4- C_3N_4 appear at 454 nm and the intensity of the latter is considerably low compared to g-C_3N_4. The lower PL intensity is an indication of the lower recombination of electron-hole pairs.[51, 52] Pristine C_3N_4 showed higher PL intensity and thereby a lower photocatalytic activity. The recombination of photogenerated charge carriers was inhibited in the heterostructure prepared, contributing to the enhancement of photocatalytic efficiency through a plausible mechanism as discussed below. The mechanical mixture indicated a slight decrease in the PL intensity compared to that of C_3N_4 due to the incorporation of 4 % Co_3O_4.

Photocatalytic mechanism

Based on the results of active species trapping and PL measurements, a possible mechanism of the degradation is shown in Figure 14. g-C_3N_4 is an n-type semiconductor and Co_3O_4 is ascertained to be a p-type semiconductor. The

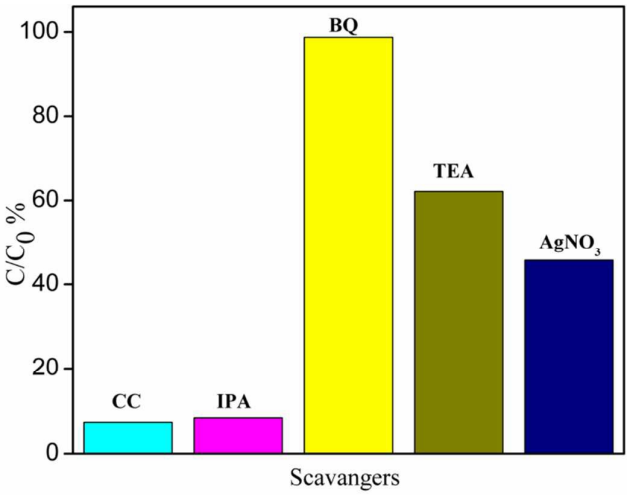

Fig. 12 Results of species trapping experiment performed using IPA, TEA, BQ, and $AgNO_3$.

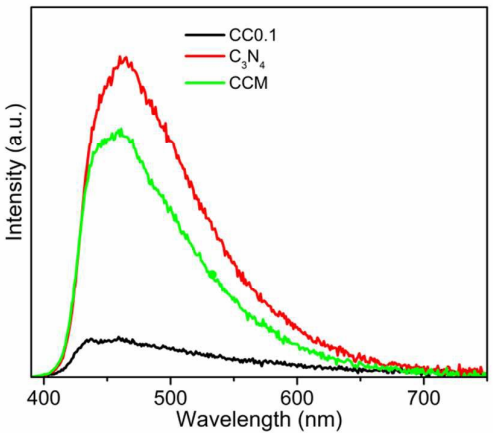

Fig. 13 PL spectra of g-C_3N_4 Co_3O_4- C_3N_4 (CC) and mechanical mixture CCM.

Interface of Co_3O_4-C_3N_4 composite thus works as a p-n heterojunction. The valence band edge potential and conduction band edge potential of semiconductor is calculated using Mulliken electronegativity theory as shown in the equation.[32]

$$E_{VB} = \chi - E^e + 0.5Eg \quad \text{Equation (2)}$$

$$E_{CB} = E_{VB} - E_g \quad \text{Equation (3)}$$

where E_{VB}, E_{CB} are the valence band edge potential and conduction band edge potential respectively. χ is the electronegativity of the semiconductor in Mulliken's scale. E^e and Eg presented the energy of free electrons on the hydrogen scale (4.5 eV vs. NHE) and the band gap of semiconductors respectively. χ values for Co_3O_4 and C_3N_4 are 5.903 and 4.64 respectively.[28, 30, 51] Bandgap energy of the p-type Co_3O_4 is found to be 2.07 eV where as for the n- type C_3N_4 is 2.7 eV. From the above formula, the E_{VB} and E_{CB} values of both semiconductors are estimated and shown in table 3.

According to the above results, the band position of C_3N_4 and Co_3N_4 before having any contact is shown in Figure 14 a. The Fermi level of the n-type C_3N_4 is located near the conduction band (CB) while that of p-type Co_3O_4 is located near the valence band (VB). In the, a p-n junction thus created the CB potential of C_3N_4 is more negative and the, electrons will therefore diffuse from the CB to the CB of Co_3O_4 leaving a negative charge accumulation in Co_3O_4. On the other hand the diffusion of holes from the VB of Co_3O_4 to VB of C_3N_4 provides a positive charge accumulation, near the vicinity of the

Table 3. The absolute electronegativity, band gap energy, valence and conduction band edges of Co_3O_4 and C_3N_4.

Semiconductor	Absolute electronegativity (χ)	Bandgap energy (eV)	Valence band potential E_{VB} (eV)	Conduction band potential E_{CB} (eV)
Co_3O_4	5.903	2.07	2.48	0.41
C_3N_4	4.64	2.70	1.5	-1.22

View Article Online
DOI: 10.1039/C6EN00410E
ARTICLE Journal Name

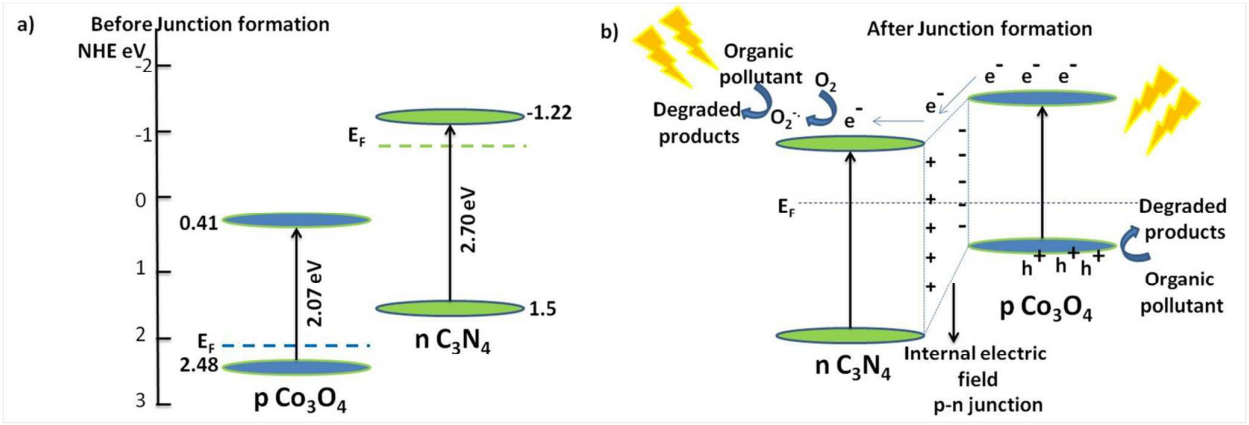

Fig. 14 a) Band alignment of p-type Co_3O_4 and n-type C_3N_4 before junction formation, b) band alignment and photocatalytic mechanism of Co_3O_4-C_3N_4 p-n nano heterojunction.

junction. As reported earlier, the Fermi level equilibration of the two semiconductors leads to an internal electric field and hence the charge diffusion in either side, which in turn shifts the band positions of the two semiconductors.[28, 31-33, 53] The band positions of the n-type C_3N_4 is down shifted along with the Femi level where as the band positions of the p-type Co_3O_4 is up shifted along with the Fermi levels allowing the CB of Co_3O_4 to be more negative. Upon sunlight irradiation, electrons in both the visibly active semiconductors get photoexcited to their respective CB leaving holes in the VB. At the junction interface, since the CB of Co_3O_4 is more negative, electrons are diffused to CB of C_3N_4 leaving holes in the CB of Co_3O_4 (Figure 14 b). Thus the formation of p-n heterojunction serves to separate the charge carriers as much as possible through the formation of internal electric field and hence the charge recombinations are prohibited in the junction. As shown in the ROS scavenging trials above (Figure 12), the electrons diffused to the CB of C_3N_4 react with oxygen producing superoxide anion radicals, which degrade the organic pollutant efficiently while holes in the VB directly degrade organic pollutants. Over all, the high surface area, increased visible light absorption, and formation of an effective nano p-n junction in Co_3O_4-C_3N_4 served to outperform the photocatalytic degradation of the individual components. Additionally, the nanodimension and highly dispersed states of Co_3O_4 suppressed the interfacial charge recombination thereby enhancing the charge separation.

A survey of the published works employing Co_3O_4 as the second phase in C_3N_4 matrix, as presented in Table S2, indicates an edge for the current synthesis methodology over the reported ones. The facile one-pot approach of co-pyrolysing the constituent raw materials in air atmosphere results in ultrafine dispersions of Co_3O_4 nanoparticles in C_3N_4 sheets leading to a tenfold increase in surface area and a nearly homogeneous distribution of Co_3O_4 phase. The silica templating method commonly employed for the preparation of mesoporous g-C_3N_4 necessitates an acid etching step, to remove silica, making the process environmentally non-friendly. Moreover, the formation of intimate interfaces of p-n heterojunctions favours enhanced photophysical properties thereby reducing exciton recombinations and improving the photocatalytic behavior. It is also to be noted that the developed photocatalysts are capable of simultaneously degrading multiple pollutants from a mixture of contaminants that are believed to be emerging environmental threats. A direct comparison of the photocatalytic efficiencies is however not feasible owing to differences (type of pollutant, concentration of catalyst etc) in the degradation studies.

Conclusions

The Co_3O_4-C_3N_4 a p-n heterojunction composite, prepared using a one-pot synthesis methodology resulted in 10 fold enhancement of surface area compared to pristine C_3N_4 and resulted in improved visible light absorption. Ultrafine Co_3O_4 (10-15nm in size) particles are seen dispersed in g-C_3N_4 sheets leading to the formation of p-n nano heterojunctions with appropriate band bending. This has resulted in reduced exciton recombinations as confirmed by mass normalised PL measurements. The radical scavenging experiments revealed that the active species employed in the photo induced degradation processes are superoxide anions, holes and electrons. The C_3N_4-4 wt % Co_3O_4 composite exhibited enhanced photocatalytic activity by effectively degrading a mixture of tetracycline and methylene blue under sunlight irradiation.

Acknowledgements

The Mr. Kiran Mohan and Mrs. Soumya Valsalam are thankfully acknowledged for the HRTEM micrographs and SEM EDS mapping respectively. Ms. Athira A. S. is gratefully acknowledged fir the COD analysis. The authors are grateful to Council of Scientific and Industrial Research (CSIR, Government

View Article Online
DOI: 10.1039/C6EN00410E

of India) for the 12thfive year plan project on "IntelCoat" (CSC0114). Author S P thanks CSIR for the research fellowship.

References

1 N. Bhandary, A. P. Singh, S. Kumar, P. P. Ingole, G. S. Thakur, A. K. Ganguli and S. Basu, ChemSusChem, 2016, DOI: 10.1002/cssc.201600740.
2 M. Zhang, W. Jiang, D. Liu, J. Wang, Y. Liu, Y. Zhu and Y. Zhu, Appl. Catal.B, 2016, 183, 263-268.
3 H. Wang, L. Zhang, Z. Chen, J. Hu, S. Li, Z. Wang, J. Liu and X. Wang, Chem. Soc. Rev., 2014, 43, 5234-5244.
4 V. Kalarivalappil, C. M. Divya, W. Wunderlich, S. C. Pillai, S. J. Hinder, M. Nageri, V. Kumar and B. K. Vijayan, Catal. Lett., 2016, 146, 474-482.
5 V. S. Smitha, K. V. Baiju, P. Perumal, S. Ghosh and K. G. Warrier, Eur. J. Inorg. Chem., 2012, 2012, 226-233.
6 Y. Wang, R. Shi, J. Lin and Y. Zhu, Energy Environ. Sci., 2011, 4, 2922-2929.
7 D. Malwal and P. Gopinath, Environ. Sci.: Nano, 2015, 2, 78-85.
8 Y. Bai, L. Ye, L. Wang, X. Shi, P. Wang and W. Bai, Environ. Sci.: Nano, 2016, 3, 902-909.
9 L. Ye, Y. Su, X. Jin, H. Xie and C. Zhang, Environ. Sci.: Nano, 2014, 1, 90-112.
10 L. Yu, H. Wang, Y. Zhang, B. Zhang and J. Liu, Environ. Sci.: Nano, 2016, 3, 28-44.
11 X. Wang, K. Maeda, A. Thomas, K. Takanabe, G. Xin, J. M. Carlsson, K. Domen and M. Antonietti, Nat. Mater., 2009, 8, 76-80.
12 W.-J. Ong, L.-L. Tan, Y. H. Ng, S.-T. Yong and S.-P. Chai, Chem. Rev., 2016, 116, 7159-7329.
13 J. Liu, H. Wang and M. Antonietti, Chem. Soc. Rev., 2016, 45, 2308-2326.
14 B. Wang, H. Wang, X. Zhong, Y. Chai, S. Chen and R. Yuan, Chem. Commun., 2016, 52, 5049-5052.
15 G. Dong, Y. Zhang, Q. Pan and J. Qiu, J. Photochem. Photobiol. C: Photochem. Rev., 2014, 20, 33-50.
16 Z. Zhang, K. Liu, Z. Feng, Y. Bao and B. Dong, Sci. Rep., 2016, 6, 19221.
17 F. Guo, J. Chen, M. Zhang, B. Gao, B. Lin and Y. Chen, J. Mater. Chem. A, 2016, 4, 10806-10809.
18 A. A. S. Nair and R. Sundara, J. Phys. Chem. C, 2016, 120, 9612-9618.
19 K. Takanabe, K. Kamata, X. Wang, M. Antonietti, J. Kubota and K. Domen, Phys. Chem. Chem. Phys., 2010, 12, 13020-13025.
20 S. Cao, J. Low, J. Yu and M. Jaroniec, Adv. Mater., 2015, 27, 2150-2176.
21 B. Zeng, L. Zhang, X. Wan, H. Song and Y. Lv, Sens. Actuator B-Chem., 2015, 211, 370-376.
22 S.-W. Cao, X.-F. Liu, Y.-P. Yuan, Z.-Y. Zhang, Y.-S. Liao, J. Fang, S. C. J. Loo, T. C. Sum and C. Xue, Appl. Catal.B, 2014, 147, 940-946.
23 J. Chen, S. Shen, P. Guo, M. Wang, P. Wu, X. Wang and L. Guo, Applied Catalysis B: Environmental, 2014, 152–153, 335-341.
24 L. Huang, H. Xu, Y. Li, H. Li, X. Cheng, J. Xia, Y. Xu and G. Cai, Dalton Trans., 2013, 42, 8606-8616.
25 J.-X. Sun, Y.-P. Yuan, L.-G. Qiu, X. Jiang, A.-J. Xie, Y.-H. Shen and J.-F. Zhu, Dalton Trans., 2012, 41, 6756-6763.
26 X. Xiao, J. Wei, Y. Yang, R. Xiong, C. Pan and J. Shi, ACS Sustainable Chem. Eng., 2016, 4, 3017-3023.
27 K. Yang, C. Meng, L. Lin, X. Peng, X. Chen, X. Wang, W. Dai and X. Fu, Catal. Sci. Technol., 2016, 6, 829-839.
28 X. Chang, T. Wang, P. Zhang, J. Zhang, A. Li and J. Gong, J. Am. Chem. Soc., 2015, 137, 8356-8359.
29 L. Zhang, Z. Gao, C. Liu, Y. Zhang, Z. Tu, X. Yang, F. Yang, Z. Wen, L. Zhu, R. Liu, Y. Li and L. Cui, J. Mater. Chem. A, 2015, 3, 2794-2801.
30 J. Wang and F. E. Osterloh, J. Mater. Chem. A, 2014, 2, 9405-9411.
31 Z. He, Y. Shi, C. Gao, L. Wen, J. Chen and S. Song, J. Phys. Chem., 2014, 118, 389-398.
32 J. Jiang, X. Zhang, P. Sun and L. Zhang, J. Phys. Chem. C, 2011, 115, 20555-20564.
33 D. Jiang, L. Chen, J. Zhu, M. Chen, W. Shi and J. Xie, Dalton Trans., 2013, 42, 15726-15734.
34 J. Ran, J. Zhang, J. Yu, M. Jaroniec and S. Z. Qiao, Chem. Soc. Rev., 2014, 43, 7787-7812.
35 P. Qiu, H. Chen and F. Jiang, RSC Adv., 2014, 4, 39969-39977.
36 J. Zhang, M. Grzelczak, Y. Hou, K. Maeda, K. Domen, X. Fu, M. Antonietti and X. Wang, Chem. Sci., 2012, 3, 443-446.
37 C. Han, L. Ge, C. Chen, Y. Li, X. Xiao, Y. Zhang and L. Guo, Appl. Catal.B, 2014, 147, 546-553.
38 C. Fettkenhauer, X. Wang, K. Kailasam, M. Antonietti and D. Dontsova, *J. Mater. Chem. A*, 2015, **3**, 21227-21232
39 D. Su, S. Dou and G. Wang, Sci. Rep. 2014, 4, 5767.
40 H. Wang, C. Chen, Y. Zhang, L. Peng, S. Ma, T. Yang, H. Guo, Z. Zhang, D. S. Su and J. Zhang, Nat. Commun., 2015, 6.
41 G. Zhang, J. Zhang, M. Zhang and X. Wang, J. Mater. Chem., 2012, 22, 8083-8091.
42 W. Jiang, W. Luo, R. Zong, W. Yao, Z. Li and Y. Zhu, Small, 2016, 12, 4370-4378.
43 G. Zhang, S. Zang, L. Lin, Z.-A. Lan, G. Li and X. Wang, ACS Appl. Mater. Interfaces, 2016, 8, 2287-2296.
44 Y. Li and N. Chopra, J. Catal., 2015, 329, 514-521.
45 D. K. Mishra, J. Mohapatra, M. K. Sharma, R. Chattarjee, S. K. Singh, S. Varma, S. N. Behera, S. K. Nayak and P. Entel, J. Magn. Magn. Mater.,2013, 329, 146-152.
46 Y. Wang, X. Wang and M. Antonietti, Angew. Chem., Int. Ed., 2012, 51, 68-89.
47 P. Niu, L. Zhang, G. Liu and H.-M. Cheng, Adv. Funct. Mater., 2012, 22, 4763-4770.
48 M. Long, W. Cai, J. Cai, B. Zhou, X. Chai and Y. Wu, J. Phys. Chem. B, 2006, 110, 20211-20216.
49 S. Samanta, S. Martha and K. Parida, ChemCatChem, 2014, 6, 1453-1462.
50 C. Liu, G. Wu, J. Chen, K. Huang and W. Shi, *New J. Chem.*, 2016, **40**, 5198-5208.
51 P. Suyana, K. R. Sneha, N. N. Balagoapl, V. Karunakaran, A. P. Mohamed, K. G. K. Warrier and U. S. Hareesh, RSC Adv., 2016, 6, 17800-17809.
52 Y. Wang, X. Bai, H. Qin, F. Wang, Y. Li, X. Li, S. Kang, Y. Zuo and L. Cui, ACS Appl. Mater. Interfaces, 2016, 8, 17212-17219.
53 Y. Ao, K. Wang, P. Wang, C. Wang and J. Hou, Dalton Trans., 2016, 45, 7986-7997.

View Article Online
DOI: 10.1039/C6EN00410E

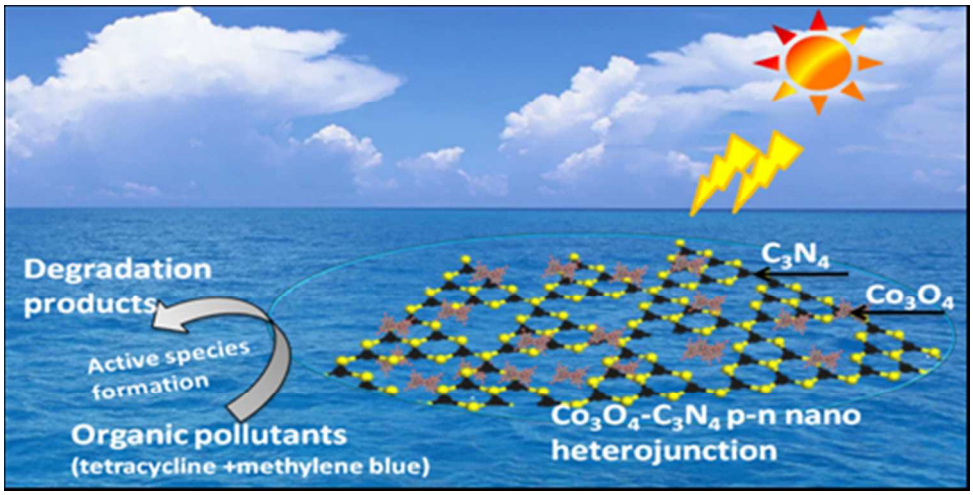

81x40mm (150 x 150 DPI)